Simulating flexible fiber suspensions using a scalable immersed boundary algorithm[☆]

Jeffrey K. Wiens, John M. Stockie[*]

Department of Mathematics, Simon Fraser University, 8888 University Drive, Burnaby, BC, Canada, V5A 1S6

Highlights

- We propose a new algorithm for simulating suspensions of flexible fibers on distributed-memory clusters.
- Our immersed boundary framework captures the full two-way interaction between fluid and flexible fibers.
- The algorithm employs a new pseudo-compressible fluid solver recently proposed by Guermond and Minev.
- Numerical results are validated against the experimental results of S.G. Mason and co-workers.

Abstract

We present an approach for numerically simulating the dynamics of flexible fibers in a three-dimensional shear flow using a scalable immersed boundary (IB) algorithm based on Guermond and Minev's pseudo-compressible fluid solver. The fibers are treated as one-dimensional neutrally-buoyant Kirchhoff rods that resist stretching, bending, and twisting, within the *generalized IB* framework. We perform a careful numerical comparison against experiments on single fibers performed by S.G. Mason and co-workers, who categorized the fiber dynamics into several distinct orbit classes. We show that the orbit class may be determined using a single dimensionless parameter for low Reynolds flows. Lastly, we simulate dilute suspensions containing up to hundreds of fibers using a distributed-memory computer cluster. These simulations serve as a stepping stone for studying more complex suspension dynamics involving aggregation of fibers (or flocculation) and particle sedimentation due to added mass.

[*] Corresponding author.
E-mail addresses: jwiens@sfu.ca (J.K. Wiens), jstockie@sfu.ca (J.M. Stockie).
URLs: http://www.jkwiens.com/ (J.K. Wiens), http://www.math.sfu.ca/~stockie (J.M. Stockie).

1. Introduction

The behavior of long, flexible fibers in a suspension plays an important role in many applications, including pulp and paper manufacture, polymer melts, and fiber-reinforced composite materials [1,2]. The dynamics of such suspensions depend heavily on the shape and flexibility of the individual fibers as well as the interactions between fibers. Because of the complexity of the fiber motion in suspensions, many researchers have developed numerical methods that afford valuable insight into both individual fiber dynamics and the resulting aggregate suspension rheology [3,4,2]. These simulations can complement physical experiments by providing information that is not easily obtained through direct measurement.

In this paper, we develop an approach for simulating a suspension of flexible fibers that is based on the immersed boundary (IB) method [5], which is a mathematical framework originally developed by Peskin [6] to capture the two-way interaction between a fluid and an immersed deformable structure. Here, the fluid deforms the elastic structure while the structure exerts forces onto the fluid. The IB method has been used to study a wide variety of biological and engineering applications including blood flow through heart valves [7,6], cell growth and deformation [8], jellyfish locomotion [9], evolution of dry foams [10] and parachute aerodynamics [11].

We treat the flexible fibers as one-dimensional Kirchhoff rods [12] described using the *generalized IB framework* developed by Lim et al. [13]. In this approach, the fibers are represented as 1D space curves using a moving Lagrangian coordinate, wherein at each Lagrangian point an orthonormal triad of vectors describes the orientation and "twist state" of the rod. This permits the fiber to generate not only a force but also a torque that is applied to the surrounding fluid.

The primary objective of this paper is to develop an efficient methodology for simulating suspensions containing a large number of flexible fibers. Since solving the full fluid–structure interaction problem comes at the expense of additional computational work, the underlying parallel algorithm is purposely designed to scale efficiently on distributed-memory computer clusters. This permits non-dilute suspensions to be simulated efficiently by spreading the work over multiple processors. The numerical algorithm is based on the work of Wiens and Stockie [14] who implemented a pseudo-compressible fluid solver developed by Guermond and Minev [15,16] in the IB framework. We extend this original algorithm to use the Eulerian–Lagrangian discretization employed by Griffith and Lim [17] which employs a predictor–corrector procedure to evolve the immersed boundary. Here, two separate force spreading and velocity interpolation steps are applied at each time step which improves the spatial convergence rate of the method.

We begin in Section 2 by reviewing theoretical and experimental results in the literature pertaining to the hydrodynamics of suspensions containing flexible fibers, as well as discussing several prominent computational approaches. In Sections 3 and 4, we state the governing equations underlying our IB model for fluid–fiber interaction, as well as the numerical algorithm used to approximate these equations. In Section 5, we present simulations of fiber dynamics in both single- and multi-fiber systems, and compare these results to previously published experimental work.
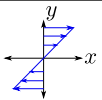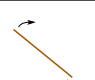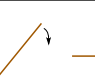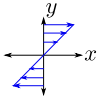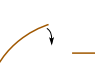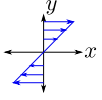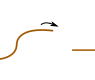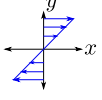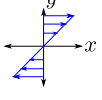
2. Background: pulp fibers

2.1. Theory and experiments

Theoretical investigations of the dynamics of fibers in a shear flow date back to Jeffery in the 1920s [18], who derived an analytical solution for the motion of a single rigid, neutrally-buoyant ellipsoidal particle immersed in an incompressible Newtonian fluid (specifically, in a Stokes flow). Jeffery found that such a fiber rotates with a well-defined periodic orbit having constant period but non-uniform angular velocity. It was later shown by Bretherton [19] that Jeffery's analytical solution could be extended to more general axisymmetric particles with non-elliptical cross-sections by replacing the ellipsoidal aspect ratio a_r by an effective aspect ratio a_r^*.

Although the theory for rigid fiber dynamics is relatively well-developed, far less is known about fibers that experience significant bending. For this reason, experimental observations are of critical importance in understanding the dynamics and rheology of suspensions containing flexible fibers. Unlike rigid fibers, flexible fibers undergo a much wider and richer range of motion when subjected to a background linear shear flow given with velocity field $\boldsymbol{u} = (Gy, 0, 0)$. This problem was studied in the pioneering work of Mason and co-workers [20–22] who categorized the fiber dynamics into several distinct orbit classes. When motions are confined to the xy-plane, fiber dynamics fall into one of four orbit classes – rigid, springy, flexible, and complex rotations – which are illustrated in Table 1. The experiments of Mason et al. involved primarily synthetic fibers (made of rayon and dacron) immersed in highly viscous fluids (such as corn syrup) although their original motivation was the application to natural wood pulp fiber suspensions.

Table 1
Two-dimensional orbit classes for flexible fibers whose unstressed state is intrinsically straight.
Source: Adapted from Forgacs et al. [22].

	Orbit class	
I	Rigid rotation	
II	Springy rotation	
IIIA	Loop or S turn	
IIIB	Snake turn	
IV	Complex rotation	

These experiments on fiber suspensions demonstrate that varying either the hydrodynamic drag force or the fiber flexibility governs the transition between the various planar orbit classes. In class I orbits, the fiber remains rigid and rotates as predicted by Jeffery's equation. When a small flexibility is introduced into the fiber, it undergoes a springy rotation (class II) in which it bends into a shallow arc as it rotates outside the horizontal plane of shear. When the fiber flexibility is increased, it experiences significant deformations that take the form of *S turns* (class IIIA) or *snake turns* (class IIIB). Note that S turns require a high degree of initial symmetry so that snake turns are actually far more prevalent in actual suspensions [20,21]. When the fiber flexibility is increased even further, the fiber may never straighten out as it returns to the horizontal, in which case the orbit is classified as a complex rotation (class IV). For the largest values of flexibility encountered in thread-like synthetic fibers, the fiber can transition beyond the class of complex rotations and undergo convoluted self-intersections as observed by Forgacs and Mason [21] in experiments.

In many cases, the fiber rotation is not constrained to the xy-plane but instead undergoes a genuinely three-dimensional orbit that protrudes or "buckles" out along the z-direction, although the xy-projection of the fiber may still belong to one of the planar orbit classes I–IV described above. Note that real suspensions such as wood pulp also contain irregularly-shaped fibers that are either intrinsically curved or contain kinks or other non-uniformities; consequently, fiber orbital dynamics in such suspensions are not necessarily confined to these idealized orbit classes. Indeed, the experiments of Arlov et al. [20] were used to classify a much broader class of genuinely three-dimensional orbits for wood pulp fibers having an intrinsic curvature.

We close this discussion by defining a dimensionless parameter that can be used to conveniently classify and predict the orbit class to which a specific fiber belongs. For low Reynolds number shear flow (with $Re \lesssim 1$), the hydrodynamic drag force experienced by a fiber oriented perpendicular to the plane of shear can be estimated by

$$F_d = \mu G D, \tag{1}$$

where μ is the fluid viscosity, G is the shear rate, and D is the diameter of the fiber [23]. By balancing this drag force with the corresponding fiber bending force, a single dimensionless parameter can be derived that captures the fiber flexibility [24]

$$\chi = \frac{\mu D G L^3}{EI}, \tag{2}$$

where L is the fiber length, E is Young's modulus of the material, and I is moment of area in the plane of bending. The parameter χ may also be interpreted as a ratio of fiber deflection to fiber length. In a series of 2D numerical

simulations [25], the parameter χ was shown to provide a useful measure of fiber flexibility that characterizes each orbit class over a wide range of fluid and fiber parameters. This dimensionless flexibility parameter has also appeared in the computational studies of Ross and Klingenberg [26] (where they referred to it as a dimensionless shear rate) and Wherrett et al. [27] (where χ^{-1} is called a bending number).

2.2. Overview of computational approaches

A popular class of numerical methods for simulating flexible fibers is the so-called *bead models* in which a flexible fiber is treated as a string of rigid beads that are linked together by flexible connectors. This approach originated with the work of Yamamoto and Matsuoka [28] who treated fibers as chains of bonded spheres that are free to stretch, bend and twist relative to each other. Their approach was extended by Ross and Klingenberg [26] who modeled fibers as chains of rigid prolate spheroids connected by ball and socket joints. The dynamics of the bead network are governed by Newton's laws through a balance of linear and angular momentum that incorporates the hydrodynamic and interparticle forces acting on each bead. More recently, Klingenberg's group has validated their model results against experiments for single fiber dynamics [29] as well as developing a multi-fiber extension that has been used to simulate flocculation [30]. A similar approach has been applied to the study of turbulent flows in which flexible fibers are suspended in air [31,32].

A significant shortcoming of Klingenberg's model and related variants [32,33,27,28] is that they fail to capture the full fluid–structure interaction in fiber suspensions. Although their approach does include the hydrodynamic force exerted by the fluid on the fiber, the fiber does not itself exert any force back onto the fluid; therefore, the fluid is a passive medium that obviously neglects any of the complex fluid dynamics that must occur in the region immediately adjacent to a dynamically deforming fiber. Several recent bead-type models have attempted to address this limitation, for example Wu and Aidun who proposed a model for rigid [34] and flexible [35] fibers that incorporates the full fluid–structure interaction using a Lattice Boltzmann approach. Similarly, Lindström and Uesaka proposed an alternative model for rigid [36] and flexible [37,38] fibers that uses the incompressible Navier–Stokes equations to model the fluid.

A completely different approach for capturing flexible fiber dynamics is based on the slender body theory [39] which exploits approximations to the governing equations based on a small fiber aspect ratio. This is the approach taken by Tornberg and Shelley [40] who studied flexible filaments in a Stokes flow by deriving a system of one-dimensional integral equations. They solved these integral equations numerically using a second-order method that also captures interactions between multiple fibers. This approach has been further extended by Li et al. [41] who used a similar methodology to investigate the problem of sedimentation (or settling) of flexible fibers. Unlike the bead models described earlier, this slender-body approach cleanly separates the fiber model from its numerical treatment, which makes the model more amenable to mathematical analysis and also permits the numerical discretization to be independently tested through convergence studies. Furthermore, because the fluid has been simplified by assuming a Stokes flow regime, these slender-body discretizations do not require a fluid grid because of the availability of numerical methods based on Green's-function solutions that greatly reduce the computational complexity. The only significant disadvantage of this approach, beside the Stokes flow restriction, is that there are as yet no results that incorporate any effects of fiber twist [42].

An alternative approach that permits simulating flexible fibers immersed in higher Reynolds flows is the immersed boundary method. This is the approach taken by Stockie and Green [25] who simulated a single flexible fiber in two dimensions using a simple representation of the fiber in terms of spring-like forces that resist stretching and bending. Stockie [43] later extended these results to a single 3D wood pulp fiber using a much more detailed and realistic model that explicitly captures the interwoven multi-layer network of cellulose fibrils making up the wood cell wall. More recently, Nguyen and Fauci studied diatom chains using the IB method with a similarly detailed fiber model [44]. The IB method properly captures the full interaction between the fluid and immersed structure by including the appropriate no-slip boundary condition along the fiber, although it does come at an additional cost. First of all, in comparison with slender-body models, the fluid solver portion of the IB algorithm can be significantly more expensive because it solves the Navier–Stokes equations on a finite difference grid. Secondly, because the IB method aims to capture the detailed fluid flow around the fiber, the fluid grid needs to be adequately refined in order to resolve details on the order of the fiber diameter, which in turn places practical limitations on the fiber aspect ratio that can be computed. Thirdly, a detailed characterization of the structure of a three-dimensional fiber such as in [44,43] typically requires thousands of IB points to resolve and is therefore computationally impractical for simulating semi-dilute suspensions of multiple fibers.

In this paper, we apply the IB approach to simulate flexible fibers, and we have chosen to treat each fiber instead as a one-dimensional Kirchhoff rod that resists stretching, bending and twisting, as described in the generalized IB method of Lim et al. [13]. Additionally, we employ a highly scalable implementation of the generalized IB algorithm [14] that spreads the computational work over a large number of processors, thereby permitting us to simulate hydrodynamic interactions in suspensions containing large numbers of flexible fibers.

3. Governing equations

Consider a Newtonian, incompressible fluid that fills a rectangular domain Ω having dimensions $H_x \times H_y \times H_z$ and whose state is specified using Eulerian coordinates $\boldsymbol{x} = (x, y, z)$. Immersed within the fluid is a neutrally-buoyant elastic fiber of length L. The fiber is described by a one-dimensional space curve $\Gamma \subset \Omega$, parameterized by the Lagrangian coordinate $s \in [0, L]$. The spatial configuration of the rod at time t is given in parametric form as $\boldsymbol{x} = \boldsymbol{X}(s, t)$ and its orientation and "twist state" are defined in terms of the orthonormal triad of vectors $\{\boldsymbol{D}^1(s, t), \boldsymbol{D}^2(s, t), \boldsymbol{D}^3(s, t)\}$, where the third triad vector $\boldsymbol{D}^3$ remains tangent to the space curve $\boldsymbol{X}$. Note that because of numerical considerations (described shortly), $\boldsymbol{D}^3(s, t)$ is not exactly tangent to the space curve $\boldsymbol{X}$ but is rather penalized in a way that it is only approximately in the tangential direction.

The fluid velocity $\boldsymbol{u}(\boldsymbol{x}, t)$ and pressure $p(\boldsymbol{x}, t)$ at location $\boldsymbol{x}$ and time t are governed by the incompressible Navier–Stokes equations

$$\rho \left(\frac{\partial \boldsymbol{u}}{\partial t} + \boldsymbol{u} \cdot \nabla \boldsymbol{u} \right) + \nabla p = \mu \nabla^2 \boldsymbol{u} + \boldsymbol{f} + \frac{1}{2} \nabla \times \boldsymbol{n}, \tag{3}$$

$$\nabla \cdot \boldsymbol{u} = 0, \tag{4}$$

where ρ is the fluid density and μ is the dynamic viscosity (both constants). The *Eulerian* force and torque densities, $\boldsymbol{f}$ and $\boldsymbol{n}$, are written as

$$\boldsymbol{f}(\boldsymbol{x}, t) = \int_\Gamma \boldsymbol{F}(s, t) \, \Phi_w(\boldsymbol{x} - \boldsymbol{X}(s, t)) \, ds \quad \text{and} \tag{5}$$

$$\boldsymbol{n}(\boldsymbol{x}, t) = \int_\Gamma \boldsymbol{N}(s, t) \, \Phi_w(\boldsymbol{x} - \boldsymbol{X}(s, t)) \, ds, \tag{6}$$

wherein the integrals spread the *Lagrangian* force and torque densities, $\boldsymbol{F}(s, t)$ and $\boldsymbol{N}(s, t)$, onto points in the fluid. The interaction between Eulerian and Lagrangian quantities is mediated using the smooth kernel function

$$\Phi_w(\boldsymbol{x}) = \frac{1}{w^3} \, \phi\left(\frac{x_1}{w}\right) \phi\left(\frac{x_2}{w}\right) \phi\left(\frac{x_3}{w}\right), \tag{7}$$

where

$$\phi(r) = \begin{cases} \dfrac{1}{8}(3 - 2|r| + \sqrt{1 + 4|r| - 4r^2}) & \text{if } 0 \le |r| < 1, \\ \dfrac{1}{8}(5 - 2|r| - \sqrt{-7 + 12|r| - 4r^2}) & \text{if } 1 \le |r| < 2, \\ 0 & \text{if } 2 \le |r|. \end{cases} \tag{8}$$

Here, w represents an effective thickness of the rod which is set to some multiple of the fluid mesh width h; that is, $w = Ch$ for some integer multiple $C \in \mathbb{Z}^+$. Note that if $w = h$, the kernel $\Phi_w(\boldsymbol{x})$ is identical to the discrete delta function employed in many immersed boundary methods [45–47].

The rod is modeled as a Kirchhoff rod [12] using the generalized immersed boundary framework of Lim [13]. Balancing linear and angular momentum yields the Lagrangian force and torque densities

$$\boldsymbol{F} = \frac{\partial \boldsymbol{F}^{\text{rod}}}{\partial s}, \tag{9}$$

$$\boldsymbol{N} = \frac{\partial \boldsymbol{N}^{\text{rod}}}{\partial s} + \frac{\partial \boldsymbol{X}}{\partial s} \times \boldsymbol{F}^{\text{rod}}, \tag{10}$$

in terms of the internal force $\boldsymbol{F}^{\mathrm{rod}}(s, t)$ and moment $\boldsymbol{N}^{\mathrm{rod}}(s, t)$ transmitted across a segment of the rod. Internal quantities are expanded in the basis $\{\boldsymbol{D}^1, \boldsymbol{D}^2, \boldsymbol{D}^3\}$ as

$$\boldsymbol{F}^{\mathrm{rod}} = F^1 \boldsymbol{D}^1 + F^2 \boldsymbol{D}^2 + F^3 \boldsymbol{D}^3, \tag{11}$$

$$\boldsymbol{N}^{\mathrm{rod}} = N^1 \boldsymbol{D}^1 + N^2 \boldsymbol{D}^2 + N^3 \boldsymbol{D}^3, \tag{12}$$

where the coefficient functions are defined by the constitutive relations

$$N^1 = a_1 \left(\frac{\partial \boldsymbol{D}^2}{\partial s} \cdot \boldsymbol{D}^3 - \kappa_1 \right), \qquad N^2 = a_2 \left(\frac{\partial \boldsymbol{D}^3}{\partial s} \cdot \boldsymbol{D}^1 - \kappa_2 \right), \qquad N^3 = a_3 \left(\frac{\partial \boldsymbol{D}^1}{\partial s} \cdot \boldsymbol{D}^2 - \tau \right), \tag{13}$$

$$F^1 = b_1 \left(\boldsymbol{D}^1 \cdot \frac{\partial \boldsymbol{X}}{\partial s} \right), \qquad F^2 = b_2 \left(\boldsymbol{D}^2 \cdot \frac{\partial \boldsymbol{X}}{\partial s} \right), \qquad F^3 = b_3 \left(\boldsymbol{D}^3 \cdot \frac{\partial \boldsymbol{X}}{\partial s} - 1 \right). \tag{14}$$

Eqs. (13) incorporate the resistance of the rod to bending and twisting, with a_1 and a_2 being the bending moduli (about axes $\boldsymbol{D}^1$ and $\boldsymbol{D}^2$ respectively) while a_3 is the twisting modulus. The constants $(\kappa_1, \kappa_2, \tau)$ define the intrinsic twist vector of the rod where $\kappa := \sqrt{\kappa_1^2 + \kappa_2^2}$ is the intrinsic curvature and τ is the intrinsic twist in the stress-free configuration. The remaining force terms (14) act to keep the triad vector $\boldsymbol{D}^3$ approximately aligned with the tangent curve $\partial \boldsymbol{X}/\partial s$ and also penalize any stretching of the rod from its equilibrium configuration. Accordingly, the generalized IB method can be viewed as a type of penalty method in which the rod is only approximately inextensible and approximately aligned with the orthonormal triad, and the constants b_1, b_2 and b_3 play the role of penalty parameters.

The final equations required to close the system are evolution equations for the rod configuration and triad vectors

$$\frac{\partial \boldsymbol{X}}{\partial t}(s, t) = \boldsymbol{U}(s, t), \tag{15}$$

$$\frac{\partial \boldsymbol{D}^\alpha}{\partial t}(s, t) = \boldsymbol{W}(s, t) \times \boldsymbol{D}^\alpha(s, t), \tag{16}$$

where $\alpha = 1, 2, 3$, and $\boldsymbol{U}(s, t)$ and $\boldsymbol{W}(s, t)$ are the linear and angular velocities along the axis of the rod respectively. These equations require that the rod translate and rotate according to the local average linear and angular velocity of the fluid, and are interpolated in the standard IB fashion as

$$\boldsymbol{U}(s, t) = \int_\Omega \boldsymbol{u}(\boldsymbol{x}, t) \, \Phi_w(\boldsymbol{x} - \boldsymbol{X}(s, t)) \, d\boldsymbol{x}, \tag{17}$$

$$\boldsymbol{W}(s, t) = \frac{1}{2} \int_\Omega \nabla \times \boldsymbol{u}(\boldsymbol{x}, t) \, \Phi_w(\boldsymbol{x} - \boldsymbol{X}(s, t)) \, d\boldsymbol{x}. \tag{18}$$

By using the same kernel function Φ_w as in (5)–(6), we ensure that energy is conserved during the Eulerian–Lagrangian interactions [13].

3.1. Problem geometry and initial conditions

The problem geometry is illustrated in Fig. 1, showing a fiber Γ immersed in a rectangular fluid domain Ω. Periodic boundary conditions are imposed on the fluid in the x- and z-directions, while the fluid is sheared in the vertical (y) direction. The shear flow is induced by imparting a horizontal motion to the top and bottom boundaries, with the top wall moving at speed U_{top} and the bottom wall in the opposite direction at speed U_{bot}. In practice, we impose $U_{\mathrm{top}} = U_{\mathrm{bot}} := U$ and set the initial fluid velocity to the linear shear profile $\boldsymbol{u}(\boldsymbol{x}, 0) = \left(G(y - H_y/2), 0, 0 \right)$ that would develop in the absence of the fiber, with shear rate $G = 2U/H_y$. The fiber of length L is placed at the center of the fluid domain which is specified by the constant $\boldsymbol{X}_0$, and we consider three different initial configurations for the fiber:
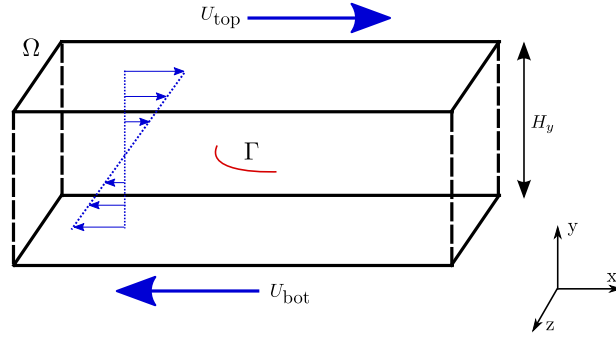
Fig. 1. Problem geometry for a single fiber Γ located at the center of a periodic, rectangular channel Ω of dimension $H_x \times H_y \times H_z$. A planar shear flow is generated by forcing the top and bottom walls to move with constant velocities $\pm U_{top}$.

Configuration 1. The fiber is initially straight and is parameterized by

$$X(s, 0) = ((\epsilon_0 + 1)s, \ 0, \ 0) + X_0,$$
$$D^1(s, 0) = (0, \ 1, \ 0),$$
$$D^2(s, 0) = (0, \ 0, \ 1),$$
$$D^3(s, 0) = (1, \ 0, \ 0),$$

where $0 \leq s < L$ and ϵ_0 is a perturbation parameter that initially stretches the fiber.

Configuration 2. The fiber is curved in the xy-plane with

$$X(s, 0) = (r_0 \cos(s/r_0 + \pi), \ r_0 \sin(s/r_0 + \pi), \ 0) + X_0,$$
$$D^1(s, 0) = (0, \ 0, \ 1),$$
$$D^2(s, 0) = (\cos(s/r_0 + \pi), \ \sin(s/r_0 + \pi), \ 0),$$
$$D^3(s, 0) = (\sin(s/r_0), \ \cos(s/r_0 + \pi), \ 0),$$

where $\alpha_b r_0 \pi \leq s < \alpha_e r_0 \pi$, and α_b and α_e are constants with $0 \leq \alpha_b < \alpha_e \leq 1$. Here, the fiber is a segment of a circle of radius r_0 lying in the xy-plane and having length $L = (\alpha_e - \alpha_b)\pi r_0$. Choosing a sufficiently large radius r_0 generates fiber with small initial curvature.

Configuration 3. Similar to Configuration 2, except that the fiber is curved in the xz-plane with

$$X(s, 0) = ((\epsilon_0 + r_0) \cos(s/r_0), \ 0, \ (\epsilon_0 + r_0) \sin(s/r_0)) + X_0,$$
$$D^1(s, 0) = (0, \ -1, \ 0),$$
$$D^2(s, 0) = (\cos(s/r_0), \ 0, \ \sin(s/r_0)),$$
$$D^3(s, 0) = (\sin(s/r_0 + \pi), \ 0, \ \cos(s/r_0)),$$

where $\alpha_b r_0 \pi \leq s < \alpha_e r_0 \pi$, and α_b and α_e are constants satisfying $0 \leq \alpha_b < \alpha_e \leq 1$.

For all three configurations, the rod has open ends so that boundary conditions are required at $s = 0$ and L. We assume that the internal force and moment vanish at the endpoints, corresponding to $F^{rod}_{-1/2} = F^{rod}_{N_s-1/2} = 0$ and $N^{rod}_{-1/2} = N^{rod}_{N_s-1/2} = 0$, which are consistent with the boundary conditions applied by Lim [48].

4. Numerical method

Here, we provide only a very brief overview of the numerical method used to solve the governing equations, while a detailed description of the method and its parallel implementation can be found in [49,14].

When discretizing the governing equations we use two separate computational grids, one each for the Eulerian and Lagrangian variables. The fluid domain is divided into an $N_x \times N_y \times N_z$, uniform, rectangular mesh where each cell has side length h. We employ a *marker-and-cell* (MAC) discretization [50] wherein the pressure is approximated at cell center points $x_{i,j,k}$ for $i, j, k = 0, 1, \ldots, N - 1$, while velocity components are located on cell faces. The Lagrangian variables are discretized at N_s uniformly-spaced points denoted by $s_\ell = \ell \Delta s$ for $\ell = 0, 1, \ldots, N_s - 1$

with $\Delta s = L/N_s$. Since our current implementation is restricted to periodic fluid domains, the top and bottom wall boundary conditions are imposed by slightly increasing the size of the fluid domain in the y-direction and introducing planes of *IB tether points* along $y = 0$ and H_y that are attached by very stiff springs to points moving at the specified velocities U_{top} and U_{bot}. We did this for convenience only, since neither the governing equations nor the fluid solver is restricted to periodic domains.

The IB equations are approximated using a fractional-step method described by Wiens and Stockie [14] in which the calculation of fluid variables is decoupled from that of the immersed boundary. For integrating the fluid equations, we use the pseudo-compressibility method developed by Guermond and Minev [15,16], which employs a directional-splitting strategy that reduces to a series of one-dimensional tridiagonal systems. These linear systems can be solved efficiently on distributed-memory clusters by combining Thomas's algorithm with a Schur-complement technique.

When integrating the rod position and orthonormal triad vectors forward in time, we use the predictor–corrector procedure devised by Griffith and Lim [17]. This differentiates our numerical method from the approach taken in [14], where an Adams–Bashforth extrapolation was used to evolve the immersed boundary in time. Although the predictor–corrector procedure introduces additional work, the expense is completely offset by allowing a much larger time step while maintaining a higher convergence rate.

Lastly, the constitutive relations (9)–(14) are discretized in the same manner as in Lim et al. [13], with the main difference being in how the orthonormal triad vectors are interpolated onto half Lagrangian steps $s_{\ell+\frac{1}{2}} = (\ell + \frac{1}{2})\Delta s$. Here, we use the Rodrigues' rotation formula as described in [49] instead of taking the principal square root used by Lim et al. [13].

If we assume that the state variables are all known at time t_n, the IB algorithm for a single time step Δt proceeds as follows.

1. Interpolate the linear and angular fluid velocities onto the rod using the delta kernel $\Phi_w(x)$ to obtain U^n and W^n.
2. Predict the rod position $X^{n+1,*}$ and orthonormal triad vectors $(D^\alpha)^{n+1,*}$ at time $t_{n+1} = (n+1)\Delta t$ to first order for $\alpha = 1, 2, 3$.
3. Calculate the Lagrangian force and torque densities, F and N, at times t_n and t_{n+1} using the discretization employed by Lim et al. [13].
4. Spread the Lagrangian force and torque densities just calculated onto fluid grid points. Then approximate the Eulerian force and torque density, $f^{n+\frac{1}{2}}$ and $n^{n+\frac{1}{2}}$, at time $t_{n+\frac{1}{2}} = (n + \frac{1}{2})\Delta t$ using an arithmetic average.
5. Integrate the incompressible Navier–Stokes equations to time t_{n+1} using $(f^{n+\frac{1}{2}} + \frac{1}{2}\nabla \times n^{n+\frac{1}{2}})$ as the external body force.
6. Correct the rod position X^{n+1} and orthonormal triad $(D^\alpha)^{n+1}$ to second order. This requires interpolating the linear and angular fluid velocity at time t_{n+1} onto the rod location.

An extensive convergence study has been performed for this algorithm in [49] that clearly shows the method converges with second-order spatial accuracy for a related problem involving a closed, twisted ring in three dimensions. For completeness, we have also included convergence results for the flexible fiber problem in Section 5.1.

5. Numerical results

5.1. Intrinsically straight fibers

We begin by considering the behavior of a single flexible fiber immersed in a shear flow, where the equilibrium fiber state is intrinsically straight (with no bend, no twist). As described earlier in Section 2, experimental observations show that such fibers are characterized by a well-defined orbital motion that can be separated into one of several distinct orbit classes according to a fiber flexibility parameter χ that captures the ratio of fiber bending force to hydrodynamic drag. This section aims to investigate the full range of these two-dimensional orbital motions.

In all simulations, we use the numerical parameters listed in Tables 2 and 4. Since the fiber motion is confined to the xy-plane, we significantly reduce the execution time of a simulation by shrinking the domain depth H_z, which allows us to run 100+ simulations in a reasonable timeframe. Note that these results are virtually identical to simulations using a larger domain ($H_z = 2$), which we confirmed through numerous computational experiments. In all simulations, we choose physical parameters that are consistent with natural (unbeaten) kraft pulp fibers, taking a fiber length of 0.1–0.3 cm and flexural rigidity of 0.001–0.07 g cm^3/s^2 [51,52]. Because fibers in our numerical simulations have

Table 2
Numerical and physical parameter values used in rigid fiber simulations.

Parameter	Symbol	Value	
Size of fluid domain Ω	$H_x \times H_y \times H_z$	$2 \times \frac{1}{2} \times 16h$	cm
Number of fluid grid points	$N_x \times N_y \times N_z$	$256 \times 64 \times 16$	
Fluid mesh width	h	$1/128$	cm
Fluid density	ρ	1.0	g/cm^3
Fluid viscosity	μ	10.0	g/(cm s)
Speed of moving plates	$U_{\text{top}} = U_{\text{bot}}$	8	cm/s
Shear rate	G	32	s^{-1}
Time step	Δt	1e − 5	s
Fiber length	L	0.3	cm
Fiber mesh width	Δs	$L/120$	cm
Bending and twisting modulus (EI)	$a_1 = a_2 = a_3$	0.7	dyne cm^2
Shear and stretch modulus	$b_1 = b_2 = b_3$	540	dyne
Fiber effective thickness	w	0.0078125	cm
Intrinsic twist vector	$(\kappa_1, \kappa_2, \tau)$	(0, 0, 0)	
Fiber length perturbation	ϵ_0	0.001	
Support of delta kernel	C	4	

diameter that is proportional to the effective thickness w, our simulated fibers are actually thicker than a natural pulp fiber. For example, we use a delta function regularization corresponding to $w \approx 80$ μm, whereas a natural pulp fiber has a diameter between 20 and 80 μm. Since the precise dependence of the simulated fiber diameter on w is unknown, we appeal to the work of Bringley and Peskin [53] where they observed that a one-dimensional array of rigid IB points has an effective numerical thickness of $D \approx 2w$. Although these results may not be strictly applicable in the present setting, this approximation is sufficient for our purposes. Any remaining discrepancy in the fiber diameter can then be accommodated for by adjusting the value of fiber drag force (see F_d from Eq. (1)).

In Figs. 3 and 4, we display snapshots of the dynamics of a fiber with initial configuration lying in the xy-plane and for six values of the dimensionless flexibility parameter χ between 0.19 and 1.125e5. As expected, the simulations exhibit a range of different orbital motions that transition between the various orbit classes (rigid, springy, flexible, complex, coiled) as the flexibility increases. We also note that within the intermediate range of χ values, we observe both S turns and snake turns depending on the symmetry of the initial fiber configuration. Despite being very rare in actual fiber suspensions, S turns turn out to be remarkably stable in our idealized setting with a planar shear flow; indeed, it is only when asymmetry is introduced in the fiber through (for example) the initial shape or a length-dependent stiffness that snake turns are observed instead of S turns. These results are consistent with those of Mason and co-workers [20,21] who observed that S turns required a high degree of symmetry that is rarely achieved in experiments. For the largest value of $\chi = 1.125$e5 in Fig. 4(c) we observe a coiled orbit with self-entanglement, and although this type of behavior is not pertinent to pulp fibers, Forgacs and Mason [21] did observe such coiling with thread-like synthetic fibers. Eventually, this fiber forms a complex writhing bundle as the fiber undergoes self-contact, but because our model does not incorporate any contact (fiber-on-fiber) forces we make no claim that these results correspond to physically accurate coiling dynamics.

To demonstrate the accuracy of our method, we present a convergence study based on simulations of a snake turn. Except for shrinking the fluid domain to $1 \times \frac{1}{2} \times 16/128$ cm and increasing the fiber bending stiffness to 3.0e − 3 dyne cm^2, the numerical parameters remain unchanged from Table 4. We estimate the convergence rate in a sequence of solution quantities q_N, q_{2N} and q_{4N} on successively finer grids as

$$\mathcal{R}[q; N] = \log_2 \left(\frac{\mathcal{E}[q; N]}{\mathcal{E}[q; 2N]} \right), \tag{19}$$

where the error

$$\mathcal{E}[q; N] = \| q_N - \mathcal{I}^{2N \to N} q_{2N} \|_2 \tag{20}$$

is measured in the discrete ℓ^2 norm and the operator $\mathcal{I}$ interpolates a solution to a coarser mesh. The finer grid simulations use the modified parameter sets ($h = 1/256$, $\Delta t = 5$e − 6, $C = 8$) and ($h = 1/512$, $\Delta t = 2.5$e − 6, $C = 16$).

Table 3
Relative errors in the discrete ℓ^2 norm for a snake turn simulation at time $t = 0.15$.

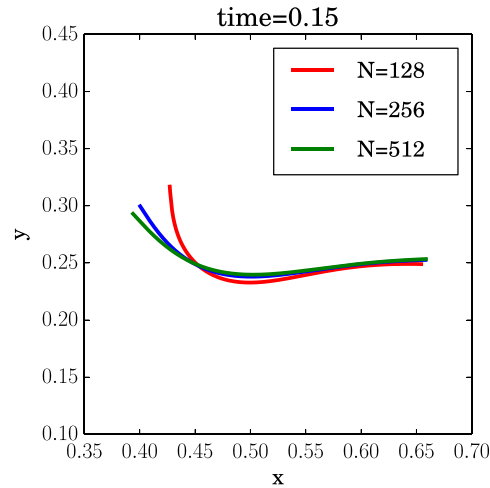|	$\mathcal{E}[\boldsymbol{u}; N] / \max |\boldsymbol{u}_{512}|$	$\mathcal{E}[p; N] / \max |p_{512}|$	$\mathcal{E}[X; N] / L$
$N = 128$	2.69e − 3	2.94e − 3	9.91e − 3
$N = 256$	1.29e − 3	1.58e − 3	2.69e − 3

Fig. 2. Fiber configuration for a snake turn simulation at three different spatial resolutions.

Table 4
Parameter modifications for the flexible fiber simulations in Figs. 3 and 4. Only those parameters that have changed relative to values indicated in Table 2 are shown here.

Orbit Class	Configuration	Parameters
Springy	2	$r_0 = 0.45, \alpha_b = 0.4, \alpha_e = 0.6, EI = 2.5e − 2,$ $\Delta s \approx 1.25e − 3, L \approx 0.282$
S turn	1	$EI = 3.0e − 3$
Snake turn	2	$r_0 = 0.45, \alpha_b = 0.4, \alpha_e = 0.6, EI = 3.0e − 3,$ $\Delta s \approx 1.25e − 3, L \approx 0.282$
Complex	2	$r_0 = 0.4, \alpha_b = 0.4, \alpha_e = 0.6, \mu = 15, EI = 1.0e−3,$ $\Delta s \approx 1.25e − 3, L \approx 0.251$
Coiled	1	$G = 64, \ \mu = 90, EI = 1.0e − 4, L = 0.5$

The errors in the computed solutions at time $t = 0.15$ s are listed in Table 3, and the corresponding convergence rates are $\mathcal{R}[\boldsymbol{u}; 128] = 1.05$, $\mathcal{R}[p; 128] = 0.90$, and $\mathcal{R}[X; 128] = 1.88$. The final fiber configuration from each of these simulations is pictured in Fig. 2 from which the convergence of the numerical solution is clear.

When the initial fiber configuration is rotated into the xz-plane, the resulting dynamics are non-planar but still follow orbits qualitatively similar to those derived by Jeffery [18]. Examples of these non-planar orbits are given in the first author's doctoral thesis [49], which show that the flexible fiber undergoes a motion consisting of a rotations in the xy-plane superimposed on a rocking motion back and forth about the z-axis in the xz-plane.

We next explore in more detail the dependence of the fiber orbit class on the dimensionless flexibility parameter χ. To this end, we perform a much larger series of simulations with varying fiber length ($L = 0.1–0.3$ cm), diameter ($D \approx 156–312$ μm), flexural rigidity ($EI = 0.001–0.1$ dyne cm^2), shear rate ($G = 20–120$ s^{-1}) and viscosity ($\mu = 0.07–100.0$ g/(cm s)) corresponding to Reynolds numbers lying in the range 0.0027–23.9. For each simulation,

(a) Rigid orbit ($\chi = 0.19$, $EI = 7.0e-1$, $L = 0.3$).

(b) Springy orbit ($\chi = 4.49$, $EI = 2.5e-2$, $L \approx 0.282$).

(c) Snake orbit ($\chi = 37.38$, $EI = 3.0e-3$, $L \approx 0.282$).
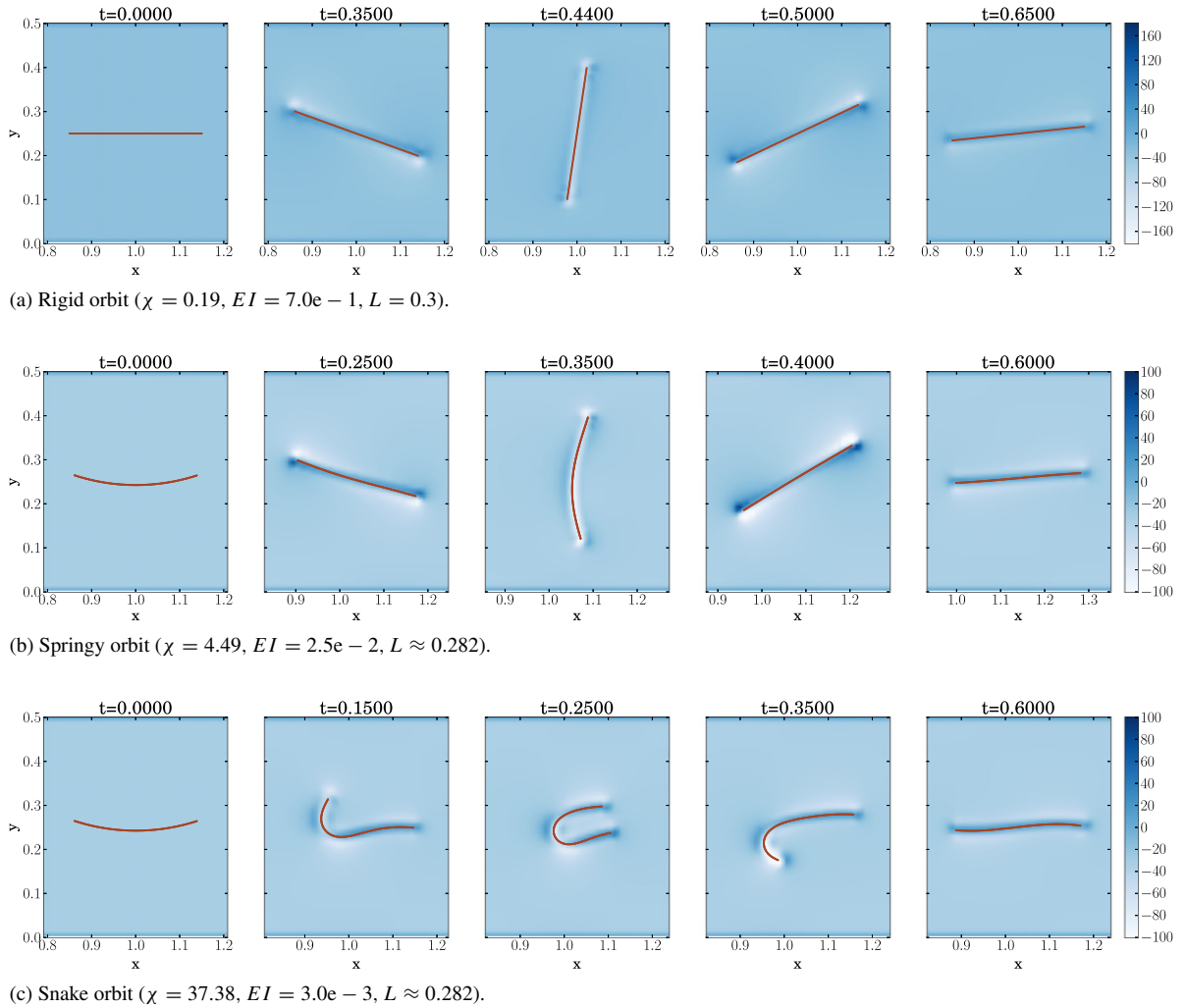
Fig. 3. Snapshots of fiber position and fluid vorticity in the xy-plane for a half-rotation in a rigid, springy and snake orbit. Parameter values are listed in Tables 2 and 4.

we assign the fiber dynamics to one of the four orbit classes I–IV by calculating the *total fiber curvature*

$$\lambda(t) = \int_0^L \left| \frac{\partial \boldsymbol{D}^3}{\partial s}(s, t) \right| ds,$$

and using the maximum curvature over a half-rotation $t_0 \leq t \leq t_1$ to apply the following criteria:

- I: The orbit is rigid if $\max_{t_0 \leq t \leq t_1} \lambda(t) < 0.4$.
- II: The orbit is springy if $0.4 \leq \max_{t_0 \leq t \leq t_1} \lambda(t) < 3.7$.
- III: The orbit is an S or snake turn if $3.7 \leq \max_{t_0 \leq t \leq t_1} \lambda(t)$ and $\lambda(t_1) < 2.5$.
- IV: The orbit is complex if $3.7 \leq \max_{t_0 \leq t \leq t_1} \lambda(t)$ and $2.5 \geq \lambda(t_1)$.

Note that S/snake turns and complex rotations have the same range of maximum curvature, and that we use the fiber curvature $\lambda(t_1)$ at the end of the half-rotation to determine whether or not the fiber has straightened out.

Simulations are depicted graphically in Fig. 5 in terms of two plots of flexural rigidity EI and drag force F_d versus dimensionless flexibility χ. Each point on the plots corresponds to a simulation using a specific choice of physical parameters, and the point type is assigned based on the orbit classification criteria above. From these two plots, it is evident that there is a clear division of orbits into classes I, II and III along vertical divisions that correspond to values of $\chi \cong 3.85$ and $\chi \cong 20.0$. The boundary between classes III and IV is not as sharply defined, but can still
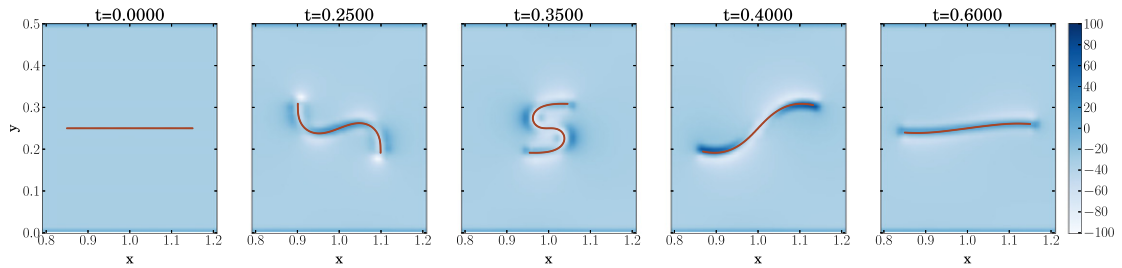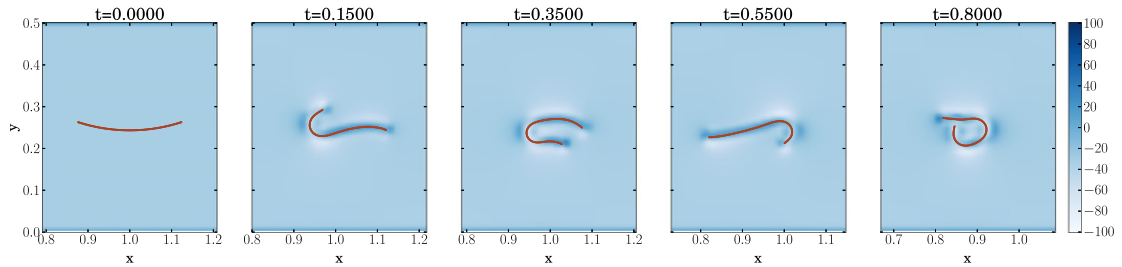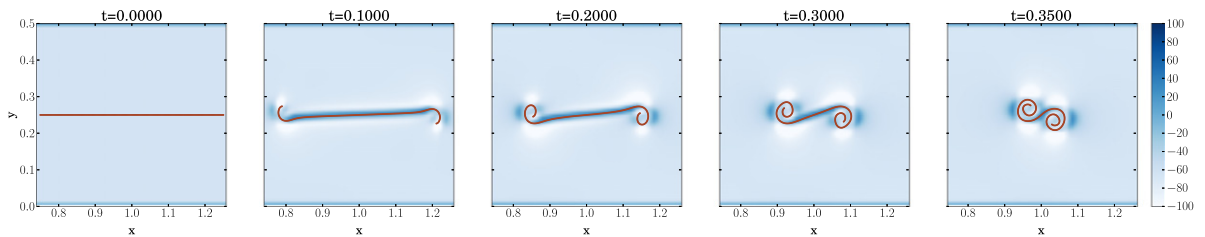
(a) S orbit ($\chi = 45.00$, $EI = 3.0e - 3$, $L = 0.3$).

(b) Complex orbit ($\chi = 119.06$, $EI = 1.0e - 3$, and $L \approx 0.251$).

(c) Coiled orbit ($\chi = 1.125e5$, $EI = 1.0e - 4$, and $L = 0.5$).

Fig. 4. Snapshots of fiber position and fluid vorticity in the xy-plane for an S turn, complex and coiled orbit. Parameter values are listed in Tables 2 and 4.

be assigned to a value of flexibility $\chi \approx 65.0$. These class boundaries are consistent with the simulations reported by Nguyen and Fauci [44]. Based on these observations, we conclude that the dimensionless flexibility χ provides a useful measure for characterizing orbit classes at the lower Reynolds numbers considered here. We note that the simulated drag rates shown in Fig. 5(b) are significantly higher than the experimental values for dacron because we are limited in terms of how high a fiber aspect ratio we can simulate owing to grid resolution. The delta function regularization introduces an effective diameter to the fibers and in order to reduce this to the same diameter of the dacron fiber in the experiments would require a fluid grid that is prohibitively expensive.

We conclude this section by performing a further comparison of our numerical simulations with the experiments of Forgacs and Mason [21] on dacron fibers in corn syrup. First of all, we list the parameters and observed orbit class for several of these experiments in Table 5. Based on values of $\chi \cdot EI$, we see that this rescaled flexibility parameter may be used to classify each orbit, assuming that EI is constant in all experiments. However, we emphasize that since Forgacs and Mason did not provide a value for the flexural rigidity (EI), we were unable to determine the value of χ explicitly.

Because these experiments were all performed with dacron fibers, we next explore further the assumption that EI is roughly constant, and also whether the experimental results are consistent with the division of orbit classes in our simulations in Fig. 5. First of all, we remark that all experimental data points are consistent with our simulations if $2.46e - 4 < EI < 3.71e - 4$ (dyne cm^2). Unfortunately, Young's modulus E for dacron is known to vary over an extremely wide range of 71.5 MPa $\leq E \leq$ 22.1 GPa between various manufacturers [54]. However, the manufacturer of the fibers used by Forgacs and Mason was identified as E.I. du Pont de Nemours and Co., and we were able to
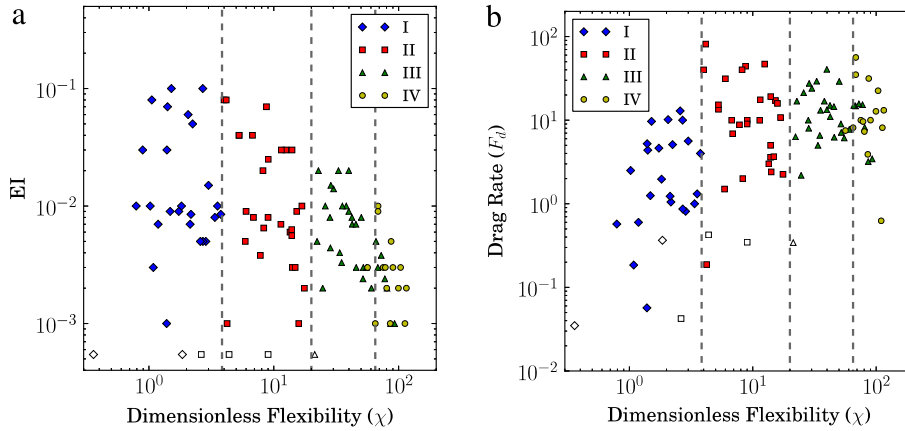
Fig. 5. Summary of all simulations showing the relationship between orbit class and different values of the dimensionless flexibility χ, flexural rigidity EI and drag rate F_d. Open markers denote the experimental data shown in Table 5 where $E = 3$ GPa.

Table 5
Experimental results obtained from Forgacs and Mason [21] for synthetic dacron fibers.

Orbit class	$\chi \cdot EI$	G (s^{-1})	μ (g/(cm s))	L (cm)	D (μm)
Rigid	1.96e − 4	3.921	11.4	0.1778	7.8
Rigid	1.01e − 3	5.143	91.2	0.1404	7.8
Springy	1.43e − 3	4.763	11.4	0.3229	7.8
Springy	2.39e − 3	5.965	91.2	0.1778	7.8
Springy	4.91e − 3	4.879	91.2	0.2418	7.8
Flexible	1.16e − 2	4.825	91.2	0.3229	7.8

find a patent filed by this company in 1969 [55] for several dacron blends that lists a much tighter range for Young's modulus of 2.0 GPa $< E <$ 3.5 GPa. Therefore, the hypothetical EI of these synthetic fibers would be between 3.63e − 4 $< EI <$ 6.36e − 4, which is consistent with our numerical results! Furthermore, most data points are still classified correctly when the EI falls outside our consistency range (2.46e − 4 $< EI <$ 3.71e − 4). To illustrate, we have plotted the experimental data in Fig. 5 using open markers, assuming $E = 3$ GPa (giving an $EI = 5.45e − 4$). Here, we observe that all experimental data are classified correctly, except for one data point. Therefore, we conclude from these results that our simulations are in excellent agreement with experimental data.

5.2. Intrinsically curved fibers

We next consider single flexible fibers that have an intrinsic curvature at equilibrium, a situation that is often encountered for natural fibers such as wood pulp. We use the base parameter values in Table 2 and simulate two cases corresponding to the modifications listed in Table 6. In both cases, the fiber is initialized as a curved segment of a circular arc with intrinsic twist vector $(\kappa_1, \kappa_2, \tau) = (1/r_0, 0, 0)$, which keeps the initial fiber configuration at equilibrium (that is, $N^1 = N^2 = N^3 = 0$ at $t = 0$).

The resulting orbits depicted in Figs. 6 and 7 clearly correspond to S- and snake-like orbits. The projections of both fibers in the xy-plane behave like the corresponding planar orbits considered in Section 5.1, but protrude into the xz-plane. These simulations reproduce similar orbital dynamics to those observed in experiments of Arlov et al. [20]. The first author's thesis [49] shows additional simulations for a fiber initially oriented along the z-direction and undergoing an additional axial spin, for which the fiber rotates around the z-axis and slightly straightens out as it rotates into the shear flow.

5.3. Multiple flexible fibers

For our last series of simulations, we consider an idealized representation of a fiber suspension that permits us to employ the domain tiling techniques described in [14]. In these computations, we simulate a $P_x \times 1 \times P_z$ array

Table 6
Parameter modifications for the flexible fiber simulations in Figs. 6 and 7. Only those parameters that have changed relative to values in Table 2 are shown here.

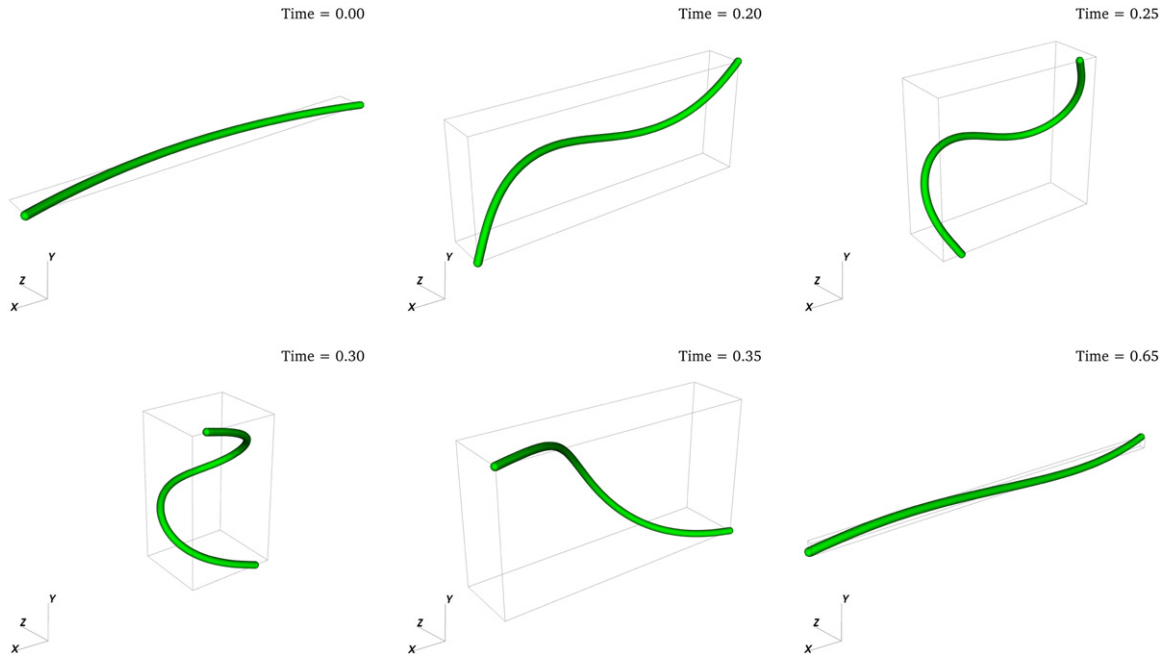| Orbit class	Configuration	Parameters
S turn	3	$H_z = 2, r_0 = 0.45, \alpha_b = 0.4, \alpha_e = 0.6, EI = 3.0e{-}3,$ $\epsilon_0 = 1e - 3, \Delta s \approx 1.25e - 3, L \approx 0.282$
Snake turn	2	$H_z = 2, r_0 = 0.45, \alpha_b = 0.4, \alpha_e = 0.6, EI = 3.0e{-}3,$ $\Theta_{xz} = \pi/16, \Delta s \approx 1.25e - 3, L \approx 0.282$

Fig. 6. Snapshots of an S turn orbit for an intrinsically curved fiber with parameters in Tables 2 and 6.

of fibers immersed in the fluid domain $\Omega = [0, P_x H_x] \times [0, H_y] \times [0, P_z H_z]$ using the boundary conditions stated in Section 3.1. The code runs in parallel on a $P = P_x \times P_z$ array of computer processors ($P_y = 1$) and the fluid domain Ω is partitioned along the x- and z-axes so that one processor labeled I, K is responsible for each subdomain $\Omega_{I,K} = [(I - 1)H_x, I H_x] \times [0, H_y] \times [(K - 1)H_z, K H_z]$, for $I = 1, 2, \ldots, P_x$ and $K = 1, 2, \ldots, P_z$. We have constructed this problem so that it can be used as a weak scalability test, wherein the local problem size is held fixed as both the number of processors and global problem size are increased. It is important to recognize that our method is in no way restricted to such idealized arrays of fibers, but rather we have employed this arrangement here in order to clearly illustrate the parallel scalability of our algorithm.

Initially, each subdomain $\Omega_{I,K}$ contains a single intrinsically-curved fiber located at its centroid, with a randomly-chosen orientation angle and whose initial shape is defined in the same manner as described earlier for Configuration 3. The numerical and physical parameters are as in Table 2 with the following modifications: $H_x = 0.421875$, $H_y = \frac{1}{2}$, $H_z = 0.3125$, $\Delta t = 5e{-}5$, $r_0 = 0.45$, $\alpha_b = 0.4$, $\alpha_e = 0.6$, $EI = 3.0e{-}3$, $\Delta s \approx 1.25e{-}3$, $L \approx 0.282$, $U_{\text{top}} = 8.5$ and $U_{\text{bot}} = 7.5$. Another difference from our earlier simulations is that the top and bottom boundaries that induce the shear flow now move at different speeds (that is, $U_{\text{top}} \neq U_{\text{bot}}$); consequently, fibers are transported across subdomain boundaries which provides a nontrivial test of our algorithm's ability to handle inter-process communication as well as changes to the IB data stored on each processor over time.

Fig. 8 presents three snapshots of the dynamics of a 16×16 array of fibers at the initial and two later times. The image at time $t = 0.25$ emphasizes the fact that all fibers spend the majority of their time aligned horizontally
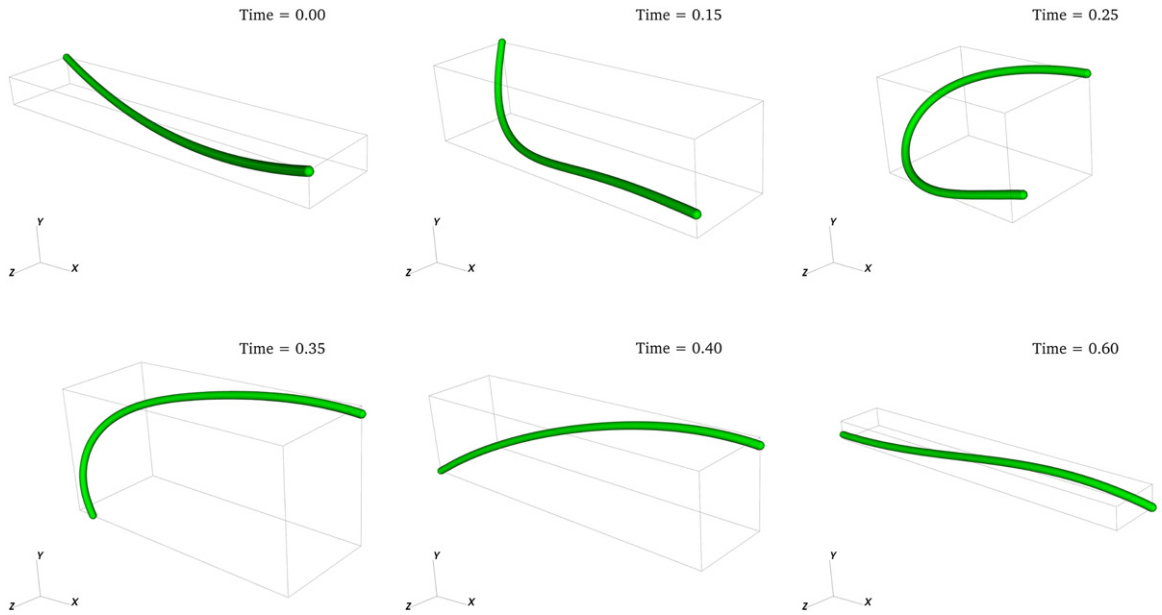
Fig. 7. Snapshots of snake turn for an intrinsically curved fiber with parameters in Tables 2 and 6.

with the shear flow (i.e., along the x-axis) and that only a small proportion of the fibers at any time instant are rotated out of the shear plane. As the suspension evolves over time, the fibers are prone to drift and cluster together, leading to development of more complex behavior such as is shown in the image at time $t = 1.80$. This last snapshot suggests that our algorithm is capable of simulating at least the initial phases of fiber flocculation involving close-range hydrodynamic interactions for a suspension with a reasonably high concentration of fibers. We note that a complete model of flocculation would require including fiber–fiber contact forces, which would be an interesting subject for future study.

The next set of results attempts to quantify the importance of including the full two-way fluid–structure interaction between fluid and fibers, relative to other more common numerical approaches that simplify or eliminate this interaction. For this purpose, we define a quantity we call the *local deviation* as

$$\mathcal{E}_{\text{rel}}(\boldsymbol{x}, t) = \frac{|\boldsymbol{u}(\boldsymbol{x}, t) - \boldsymbol{u}(\boldsymbol{x}, 0)|}{\max_{\boldsymbol{x}}(|\boldsymbol{u}(\boldsymbol{x}, 0)|)},$$

which is a local measure of the relative difference between the computed fluid velocity and the corresponding linear shear flow that would arise in the absence of any fibers. We also define a related *global deviation* from linear shear using either the ℓ^∞-norm

$$\|\mathcal{E}_{\text{rel}}(\boldsymbol{x}, t)\|_\infty = \max_{i,j,k} |\mathcal{E}_{\text{rel}}(\boldsymbol{x}_{i,j,k}, t_n)|,$$

or ℓ^1-norm

$$\|\mathcal{E}_{\text{rel}}(\boldsymbol{x}, t)\|_1 = \frac{h^3}{V} \sum_{i,j,k} |\mathcal{E}_{\text{rel}}(\boldsymbol{x}_{i,j,k}, t_n)|,$$

where V is the fluid volume. For a 25-fiber simulation computed with $(P_x, P_y, P_z) = (5, 1, 5)$ processors, we provide plots in Fig. 9 of the local deviation $\mathcal{E}_{\text{rel}}$ at time $t = 1.80$ and along two different horizontal slices. The figures have truncated the values of $\mathcal{E}_{\text{rel}}$ above the threshold 0.025 so that smaller deviations can be visualized. From these plots we observe that the local deviation is largest adjacent to the individual fibers where the no-slip condition forces the fluid to follow the deforming and rotating fibers, but that the deviation decays rapidly away from the fibers. Nonetheless, there are still significant fluid disturbances spread throughout the entire fluid domain that influence fiber motion and are related to hydrodynamic interactions between individual fibers. The corresponding global deviation values are
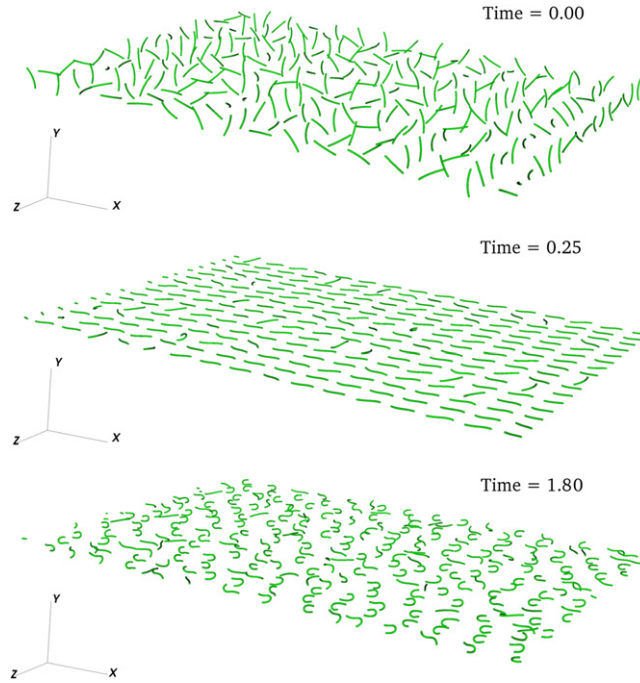
Fig. 8. A suspension of 256 intrinsically-curved fibers ($P_x = P_z = 16$) in Configuration 3. Parameters are described in Section 5.3.
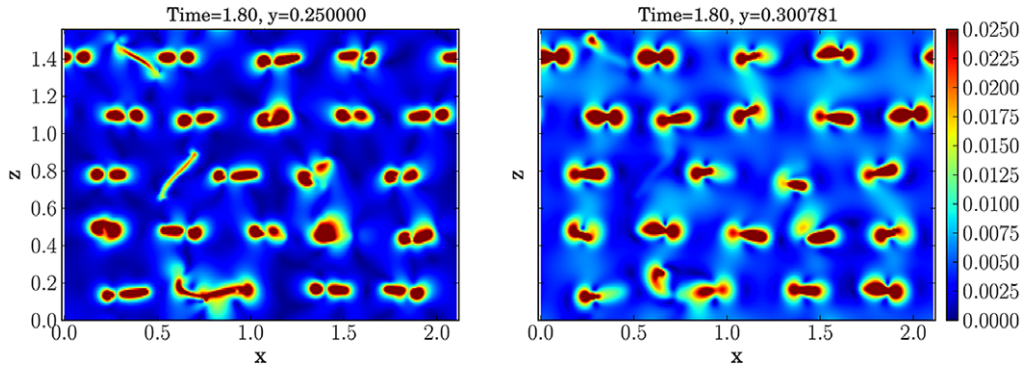

Fig. 9. Fluid deviation $\mathcal{E}_{\mathrm{rel}}$ on two horizontal planes for the 25 fiber simulation computed in Table 7. Plotted values are truncated at the threshold $\mathcal{E}_{\mathrm{rel}} = 0.025$.

$\|\mathcal{E}_{\mathrm{rel}}\|_1 = 0.0159$ and $\|\mathcal{E}_{\mathrm{rel}}\|_\infty = 0.135$ which show that relative deviations in the flow are as high as 13.5% near the fibers but that the average over the entire flow field is only about 1.6%. Other simulations using different parameters and initial conditions yield similar results (see [49]) with the average relative deviation hovering around 2% and the maximum ranging up to 40%. These results suggest that incorporating the full fluid–structure interaction into models for non-dilute suspensions is important in terms of properly capturing the dynamics of the flexible fibers. We also note that these simulations are performed at relative low values of Reynolds number and fiber concentration, and that the deviation measure will only get larger as the Reynolds number and concentration increase.

Finally, we close by investigating the parallel performance of our IB algorithm by considering simulations of different-sized suspensions of fibers on multiple processors. Based on our problem setup, the execution time would ideally stay constant as the global problem size and number of processors increase. Indeed, Table 7 shows that as the size of the fiber array (P_x, P_z) is increased, there is only a slight increase in execution time and hence our algorithm is said to be weakly scalable. We remark that our code is still not fully optimized and that the algorithm

Table 7
Weak scaling results showing the average execution time per time step (in seconds) for the multiple fiber problem. The local problem size is held fixed as the number of processors P (and global problem size) is increased. Simulations are run on the Bugaboo cluster managed by WestGrid [56].

P	(P_x, P_y, P_z)	Wall time
25	(5, 1, 5)	0.57
64	(8, 1, 8)	0.58
144	(12, 1, 12)	0.58
225	(15, 1, 15)	0.62
256	(16, 1, 16)	0.61

performance could be further improved by making enhancements such as enforcing the top/bottom wall boundary conditions directly instead of our approach of treating the walls using IB tether points.

6. Conclusions

In this paper, we have presented a parallel immersed boundary algorithm for simulating suspensions of flexible fibers, where individual fibers are modeled as Kirchhoff rods. The novelty of this work derives from its application to multi-fiber suspension flows with non-zero Reynolds number and the inclusion of the full two-way interaction between the fluid and suspended fibers. In our numerical simulations, we reproduce the full range of orbital dynamics observed experimentally by Mason and co-workers for isolated fibers immersed in a linear shear flow. When extending the results to multi-fiber suspensions, we demonstrate through a weak scalability test that the parallel scaling of our algorithm is near optimal and hence shows promise for simulating more complex scenarios such as semi-dilute suspensions and fiber flocculation.

In the future, we plan to improve on the underlying model, which will allow us to simulate more realistic fiber suspensions. First, we plan on incorporating the contact forces between fibers such as the frictional forces modeled by Schmid et al. [57]. Second, we will incorporate the effect of added fiber mass using the penalty IB method [58]. After incorporating these extensions, a more extensive comparison to experimental data would be required, comparing quantities such as the specific viscosity of the suspension [4].

References

[1] M. Keshtkar, M.C. Heuzey, P.J. Carreau, Rheological behavior of fiber-filled model suspensions: effect of fiber flexibility, J. Rheol. 53 (3) (2009) 631–650.
[2] L.H. Switzer III, D.J. Klingenberg, Rheology of sheared flexible fiber suspensions via fiber-level simulations, J. Rheol. 47 (3) (2003) 759–778.
[3] C.G. Joung, N. Phan-Thien, X.J. Fan, Direct simulation of flexible fibers, J. Non-Newton. Fluid Mech. 99 (1) (2001) 1–36.
[4] C.J.S. Petrie, The rheology of fibre suspensions, J. Non-Newton. Fluid Mech. 87 (2) (1999) 369–402.
[5] C.S. Peskin, The immersed boundary method, Acta Numer. 11 (2002) 479–517.
[6] C.S. Peskin, Flow patterns around heart valves: a numerical method, J. Comput. Phys. 10 (1972) 252–271.
[7] B.E. Griffith, X.Y. Luo, D.M. McQueen, C.S. Peskin, Simulating the fluid dynamics of natural and prosthetic heart valves using the immersed boundary method, Int. J. Appl. Mech. 1 (1) (2009) 137–177.
[8] K.A. Rejniak, R.H. Dillon, A single cell-based model of the ductal tumour microarchitecture, Comput. Math. Methods Med. 8 (1) (2007) 51–69.
[9] C. Hamlet, A. Santhanakrishnan, L.A. Miller, A numerical study of the effects of bell pulsation dynamics and oral arms on the exchange currents generated by the upside-down jellyfish *Cassiopea xamachana*, J. Exp. Biol. 214 (2011) 1911–1921.
[10] Y. Kim, Y. Seol, M.C. Lai, C.S. Peskin, The immersed boundary method for two-dimensional foam with topological changes, Commun. Comput. Phys. 12 (2) (2012) 479.
[11] Y. Kim, C.S. Peskin, 3D parachute simulation by the immersed boundary method, Comput. & Fluids 38 (6) (2009) 1080–1090.
[12] E.H. Dill, Kirchhoff's theory of rods, Arch. Hist. Exact Sci. 44 (1) (1992) 1–23.
[13] S. Lim, A. Ferent, X.S. Wang, C.S. Peskin, Dynamics of a closed rod with twist and bend in fluid, SIAM J. Sci. Comput. 31 (1) (2008) 273–302.
[14] J.K. Wiens, J.M. Stockie, An efficient parallel immersed boundary algorithm using a pseudo-compressible fluid solver, J. Comput. Phys. 281 (2015) 917–941.
[15] J.L. Guermond, P.D. Minev, A new class of fractional step techniques for the incompressible Navier–Stokes equations using direction splitting, C. R. Math. 348 (2010) 581–585.
[16] J.L. Guermond, P.D. Minev, A new class of massively parallel direction splitting for the incompressible Navier–Stokes equations, Comput. Methods Appl. Mech. Engrg. 200 (23–24) (2011) 2083–2093.

[17] B.E. Griffith, S. Lim, Simulating an elastic ring with bend and twist by an adaptive generalized immersed boundary method, Commun. Comput. Phys. 12 (2) (2012) 433.

[18] G.B. Jeffery, The motion of ellipsoidal particles immersed in a viscous fluid, Proc. R. Soc. Lond. Ser. A 102 (715) (1922) 161–179.

[19] F.P. Bretherton, The motion of rigid particles in a shear flow at low Reynolds number, J. Fluid Mech. 14 (2) (1962) 284–304.

[20] A.P. Arlov, O.L. Forgacs, S.G. Mason, Particle motions in sheared suspensions IV. General behaviour of wood pulp fibres, Sven. Papperstidning 61 (3) (1958) 61–67.

[21] O.L. Forgacs, S.G. Mason, Particle motions in sheared suspensions X. Orbits of flexible threadlike particles, J. Colloid Sci. 14 (1959) 473–491.

[22] O.L. Forgacs, A.A. Robertson, S.G. Mason, The hydrodynamic behaviour of paper-making fibres, Pulp Pap. Mag. 59 (5) (1958) 117–128.

[23] F.M. White, Viscous Fluid Flow, Vol. 46, McGraw-Hill Higher Education, Boston, 2006.

[24] J.M. Stockie, Analysis and computation of immersed boundaries, with application to pulp fibres (Ph.D. thesis), Institute of Applied Mathematics, University of British Columbia, Vancouver, Canada, 1997. Available from https://circle.ubc.ca/handle/2429/7346.

[25] J.M. Stockie, S.I. Green, Simulating the motion of flexible pulp fibres using the immersed boundary method, J. Comput. Phys. 147 (1) (1998) 147–165.

[26] R.F. Ross, D.J. Klingenberg, Dynamic simulation of flexible fibers composed of linked rigid bodies, J. Chem. Phys. 106 (1997) 2949–2960.

[27] G. Wherrett, I. Gartshore, M. Salcudean, J. Olson, A numerical model of fibre motion in shear, in: Proceedings of the 1997 ASME Fluids Engineering Division Summer Meeting, Vancouver, Canada, June 22–26, 1997.

[28] S. Yamamoto, T. Matsuoka, A method for dynamic simulation of rigid and flexible fibers in a flow field, J. Chem. Phys. 98 (1) (1993) 644–650.

[29] P. Skjetne, R.F. Ross, D.J. Klingenberg, Simulation of single fiber dynamics, J. Chem. Phys. 107 (1997) 2108–2121.

[30] L.H. Switzer, D.J. Klingenberg, Flocculation in simulations of sheared fiber suspensions, Int. J. Multiph. Flow 30 (1) (2004) 67–87.

[31] J. Andrić, Numerical modeling of air-fiber flows (Ph.D. thesis), Department of Applied Mechanics, Chalmers University of Technology, Göteborg, Sweden, 2014.

[32] J. Andrić, S.T. Fredriksson, S.B. Lindström, S. Sasic, H. Nilsson, A study of a flexible fiber model and its behavior in DNS of turbulent channel flow, Acta Mech. 224 (2013) 2359–2374.

[33] G. Wang, W. Yu, C. Zhou, Optimization of the rod chain model to simulate the motions of a long flexible fiber in simple shear flows, Eur. J. Mech. B Fluids 25 (3) (2006) 337–347.

[34] J. Wu, C.K. Aidun, Simulating 3D deformable particle suspensions using lattice Boltzmann method with discrete external boundary force, Internat. J. Numer. Methods Fluids 62 (7) (2010) 765–783.

[35] J. Wu, C.K. Aidun, A method for direct simulation of flexible fiber suspensions using lattice Boltzmann equation with external boundary force, Int. J. Multiph. Flow 36 (3) (2010) 202–209.

[36] S.B. Lindström, T. Uesaka, A numerical investigation of the rheology of sheared fiber suspensions, Phys. Fluids 21 (2009) 083301.

[37] S.B. Lindström, T. Uesaka, Simulation of the motion of flexible fibers in viscous fluid flow, Phys. Fluids 19 (11) (2007) 113307.

[38] S.B. Lindström, T. Uesaka, Simulation of semidilute suspensions of non-Brownian fibers in shear flow, J. Chem. Phys. 128 (2) (2008) 024901.

[39] G.K. Batchelor, Slender-body theory for particles of arbitrary cross-section in Stokes flow, J. Fluid Mech. 44 (3) (1970) 419–440.

[40] A.K. Tornberg, M.J. Shelley, Simulating the dynamics and interactions of flexible fibers in Stokes flows, J. Comput. Phys. 196 (2004) 8–40.

[41] L. Li, H. Manikantan, D. Saintillan, S.E. Spagnolie, The sedimentation of flexible filaments, J. Fluid Mech. 735 (2013) 705–736.

[42] S.D. Olson, S. Lim, R. Cortez, Modeling the dynamics of an elastic rod with intrinsic curvature and twist using a regularized Stokes formulation, J. Comput. Phys. 238 (2013) 169–187.

[43] J.M. Stockie, Simulating the dynamics of flexible wood pulp fibres in suspension, in: Proceedings of the 16th Annual International Symposium on High Performance Computing Systems and Applications, IEEE Computer Society, 2002, p. 154.

[44] H. Nguyen, L. Fauci, Hydrodynamics of diatom chains and semiflexible fibres, J. R. Soc. Interface 11 (96) (2014) 20140314.

[45] B.E. Griffith, C.S. Peskin, On the order of accuracy of the immersed boundary method: higher order convergence rates for sufficiently smooth problems, J. Comput. Phys. 208 (1) (2005) 75–105.

[46] M.C. Lai, C.S. Peskin, An immersed boundary method with formal second-order accuracy and reduced numerical viscosity, J. Comput. Phys. 160 (2) (2000) 705–719.

[47] Y. Mori, C.S. Peskin, Implicit second-order immersed boundary methods with boundary mass, Comput. Methods Appl. Mech. Engrg. 197 (25–28) (2008) 2049–2067.

[48] S. Lim, Dynamics of an open elastic rod with intrinsic curvature and twist in a viscous fluid, Phys. Fluids 22 (2) (2010) 024104.

[49] J.K. Wiens, An efficient parallel immersed boundary algorithm, with application to the suspension of flexible fibers (Ph.D. thesis), Department of Mathematics, Simon Fraser University, Burnaby, Canada, 2014.

[50] F.H. Harlow, J.E. Welch, Numerical calculation of time-dependent viscous incompressible flow of fluid with free surface, Phys. Fluids 8 (12) (1965) 2182–2189.

[51] P.A. Tam Doo, R.J. Kerekes, A method to measure wet fiber flexibility, Tappi J. 64 (3) (1981) 113–116.

[52] P.A. Tam Doo, R.J. Kerekes, The flexibility of wet pulp fibres, Pulp Pap. Can. 83 (2) (1982) 46–50.

[53] T.T. Bringley, C.S. Peskin, Validation of a simple method for representing spheres and slender bodies in an immersed boundary method for Stokes flow on an unbounded domain, J. Comput. Phys. 227 (2008) 5397–5425.

[54] Dacron flexural modulus. WolframAlpha. Retrieved February 10, 2014 from http://www.wolframalpha.com/input/?i=dacron+flexural+modulus.

[55] O. Cope, Polymer blends of polyethylene terephthalate and alpha-olefin,alpha,beta-unsaturated carboxylic acid copolymers, March 25 1969. US Patent 3,435,093.

[56] WestGrid. QuickStart Guide to Bugaboo. Retrieved April 11, 2013 from http://www.westgrid.ca/support/quickstart/bugaboo.

[57] C.F. Schmid, L.H. Switzer, D.J. Klingenberg, Simulations of fiber flocculation: effects of fiber properties and interfiber friction, J. Rheol. 44 (3) (2000) 781–809.

[58] Y. Kim, C.S. Peskin, Penalty immersed boundary method for an elastic boundary with mass, Phys. Fluids 19 (5) (2007) 053103.